Computational Geosciences (2020) 24:1463–1482
https://doi.org/10.1007/s10596-019-09915-7

ORIGINAL PAPER

Biogeochemical cycling of heavy metals in lake sediments: impact of multispecies diffusion and electrostatic effects

Jianing Li[1] · S. Sevinç Şengör[1,2]

Received: 3 November 2017 / Accepted: 28 October 2019 / Published online: 17 June 2020

Abstract

Fate and transport of heavy metals is controlled by the biogeochemical processes in the environment. Reactive transport modeling is particularly important for capturing the complex interplay between the microbial community dynamics and redox-stratified environments. The focus of this study is to investigate the impacts of (i) multicomponent diffusion (MCD) and (ii) electrical double layer (EDL) on reactive diffusive transport of heavy metals at Lake Coeur d'Alene (LCdA) sediments. The solute benthic fluxes at LCdA sediments are controlled by diffusion, and therefore, the biogeochemical model is focused purely on diffusive transport. In diffusive transport-dominated multicomponent systems, species-specific multicomponent diffusion (i.e., Nernst-Planck representation of diffusion) and the explicit treatment of electrostatic effects can play an important role on the overall dynamics of biogeochemical cycling of metals in the system. The results of this study demonstrate that the use of single uniform diffusion coefficient for all species in purely diffusion-dominated sediments may underestimate the mobility of heavy metals undergoing complex reaction network. This outcome is further signified when explicit treatment of EDL effects is considered in addition to MCD. The simulation results also illustrate the importance of aqueous metal (bi)sulfide complexes, especially when MCD and EDL effects are implemented in reactive transport simulations, impacting the solubility and dynamics of heavy metals in diffusion-dominated systems. The competitive effects of Fe-reducing bacteria FRB and sulfate reducing bacteria SRB activities on pH and overall biogeochemical processes are also demonstrated with multispecies diffusion and explicit treatment of electrostatic effects in the system.

Keywords Reactive transport · Multispecies diffusion · Electrical double layer · Benthic sediments

1 Introduction

Lake sediments are the ultimate repository for various contaminants, including heavy metals, originating from anthropogenic activities [1, 2]. The fate and transport of heavy metals is controlled by complex biogeochemical processes occurring at the sediments. Quantification of the heavy metal dynamics in the sediments requires an understanding of the coupled geological, chemical, and microbial processes. Reactive transport models have been widely used to investigate the biogeochemical cycling of various contaminants and heavy metals in lake sediment environments [3–11]. The models have been carried out to capture the essential biogeochemical transformations coupled to transport processes, assessing the impact of various competing reactions affecting the overall heavy metal dynamics in the system [12, 13].

This study aims to build on the previous work of Sengor et al. [11] to investigate the impact of (i) multicomponent diffusion (MCD) and (ii) electrical double layer (EDL) on reactive diffusive transport of heavy metals at Lake Coeur d'Alene (LCdA) sediments. The biogeochemical model of heavy metal cycling developed by Sengor et al. [11] was based on pure diffusive transport, as the solute benthic fluxes at LCdA are controlled by diffusion. In diffusive transport-dominated multicomponent systems, Coulombic interactions between the ionic species can play an important role in determining the rates of diffusion of ions in pore water, in addition to pure Fickian processes.

MCD and EDL effects in reactive transport modeling have been studied and reported [14–23]. MCD is a transport

✉ S. Sevinç Şengör

[1] Department of Civil and Environmental Engineering, Southern Methodist University, PO Box 750340, Dallas, TX 75275-0339, USA

[2] Department of Environmental Engineering, Middle East Technical University, Dumlupınar Bulvarı No:1, Ankara 06800, Turkey

process, in which the diffusion flux of one component is influenced by the concentration of other components in the system [24]. EDL, on the other hand, is a stratified structure outside of a surface which attracts ions, dipole molecules, and particles from the environment [25]. Appelo and Wersin [14] used PHREEQC [26] to simulate the diffusion of tritium, iodide, and sodium in Opalinus clay with the consideration of diffuse double layer. The study compared the modeling results with and without MCD for solute species HTO, I, and Na, discussing how the various terms of MCD in the free pore and DDL, and retardation by ion exchange would modify the transport of these species. The study of the multicomponent diffusion of Opalinus clay was further extended for tracer elements such as Cl, Br, Sr, and Cs [15]. It was concluded that a dual porosity model was more accurate to fit $^{85}Sr^{2+}$ and $^{134}Cs^{+}$ concentration profiles, whereas $^{22}Na^{+}$, tritium, and the anions could be modeled with a homogeneous porosity structure. The geometrical factors for ionic species were different in the clay, in which cations could be quantified as a function of the fraction of free pore water in the pore space and a given anion-accessible porosity [15]. Appelo et al. [27] developed a radial diffusion model to simulate the porewater composition in a clay rock, where diffusion was calculated with explicit finite differences for a radially configured grid. The model was used to understand the complex interactions among diffusive transport, ion exchange, and calcite dissolution. Muniruzzaman and Rolle [28] investigated the impact of multicomponent ionic transport on pH in saturated porous media under flow-through conditions. The results from laboratory bench-scale experiments in homogeneous porous medium were interpreted by the 2D numerical MCD model simulations which showed a very good agreement, confirming the importance of charge effects on pH transport in porous media.

In summary, these studies demonstrate the need for dual porosity models to quantify the diffusion of differently charged solutes especially for low ionic strength porewater systems and the influence of multicomponent approach in describing transport processes. Motivated from the significance of electrochemical migration to be included in transport processes, the study presented here investigates the impact of effective diffusion coefficient of all ions, multispecies diffusion, and explicit treatment of electrostatic effects in example diffusive transport-dominated lake sediments of LCdA. The present study is the first attempt, to the authors' knowledge, to investigate the MCD and EDL impacts on reactive transport modeling of heavy metal dynamics in *a natural environment*, integrating the coupled effects of biotic reaction network including microbial-consortium biodegradation kinetics with multiple terminal electron acceptors and heavy metal sorption through a full surface complexation model. The extent of MCD and EDL effects on the overall biogeochemical processes and competing reactions affecting heavy metal cycling in lake sediments is presented, demonstrating the impacts of these processes in a natural field-scale domain, as opposed to previously studied laboratory-based idealized or homogeneous media.

2 Model structure and approach

Molecular diffusion is usually described by Fick's first law as:

$$J_i = -\varnothing D_j^* \nabla C_j \tag{1}$$

where J_j is the diffusive flux, $\varnothing$ is the porosity, D_j^* is the diffusion coefficient in the sediment, and C_j is the concentration of species in bulk solution. Integrating the diffusive fluxes over a control volume results in the Fick's second law as [29]:

$$\frac{\partial C_j}{\partial t} = -\nabla \cdot \left[J_j\right] = \nabla \cdot \left[\varnothing D_j^* \nabla C_j\right] \tag{2}$$

where $\frac{\partial C_j}{\partial t}$ is the change in concentration with time and $\nabla \cdot \left[\varnothing D_j^* \nabla C_j\right]$ is the divergence of the diffusive flux. Equations (1) or (2), however, do not consider electrostatic forces induced by species of non-zero charge and it is therefore strictly valid only for uncharged species. Therefore, electrochemical potential (Ψ) needs to be included as a transport process, where positively and negatively charged species move in a coordinated manner to maintain local charge balance. Then, the diffusion of species *j* depends on the concentration gradient of itself and other charged species in the solution. The Nernst-Planck equation (e.g., [30–32]) is most commonly used for multispecies diffusion:

$$J_j = -\varnothing D_j^* \nabla C_j - \frac{\varnothing D_j^* C_j}{RT} z_j F \nabla \Psi \tag{3}$$

where z_j is the charge of species *j*, *F* and *R* are the Faraday and gas constants, respectively, *T* is the absolute temperature, Ψ is the electrical potential, and γ is the activity coefficient of the *j*th species. According to the Nernst-Planck equation, the diffusion of ions is controlled by the concentration gradient and the electrical field created by the movement of charged species at different rates (assuming the absence of an external electrical field as commonly captured in geochemical transport codes) [33]. The full version of the Nernst-Planck equation can be derived using the gradient expressions for chemical potential, as explained in detail by, e.g., [34].

The diffusion coefficient in the sediment (D_j^*) is related to the molecular diffusion coefficient in water (D_j^0) as:

$$D_j^* = \frac{D_j^0}{\theta^2} = \frac{D_j^0}{\varnothing F} \tag{4}$$

where θ is the sediment tortuosity and F is the "formation factor," the ratio of bulk sediment resistivity to pore water resistivity. For high porosity sediments, such as LCdA sediments, F can be approximated as $\varnothing^{-3}$ [35, 36], where D_j^* becomes [36]:

$$D_j^* = \frac{D_j^0}{\varnothing^{-2}} \tag{5}$$

The simulations presented in this study are carried out with the reactive transport code PHREEQC [26]. PHREEQC is one of the few continuum-based reactive transport codes that can handle the transport of ions with an explicit treatment of an EDL. The code considers the interlayer space to be part of the EDL. The total pore space is therefore divided into two porosity domains: the microporosity (i.e., the sum of interlayer space and the EDL) and the macroporosity containing free, charge balanced water [33]. In PHREEQC, the electrical potential and species distribution in the EDL are described by a Donnan approach. This approach assumes a single potential Ψ_{EDL} in the EDL and an instantaneous equilibrium of species between the EDL and the free water (i.e., between the micro- and macroporosity, respectively). Therefore, the diffusion between micro- and macroporosity domains is not considered explicitly and the chemical potentials, μ_i, of the species are the same in the two porosities at all times:

$$\mu_i^{\mathrm{EDL}} = \mu_i \tag{6}$$

The Donnan approximation can be described as:

$$C_i^{\mathrm{EDL}} = C_i \exp\left(\frac{-z_i F \Psi_{\mathrm{EDL}}}{RT}\right) \tag{7}$$

where C_i^{EDL} and C_i are the concentrations in the micro- and macroporosity, respectively, z_i is the valence of species i, F is the Faraday constant, T is the absolute temperature, R is the ideal gas constant, and Ψ_{EDL} is the mean electrical potential in the microporosity domain. As opposed to the charge-balanced solution in the macroporosity, the microporosity solution exhibits a net charge balancing the total charge of the surfaces [33]:

$$\varnothing^{\mathrm{EDL}} \sum_i z_i C_i^{\mathrm{EDL}} = Q_S \tag{8}$$

where ϕ^{EDL} is the volume of the microporosity domain and Q_S is the total surface charge. As discussed by Alt-Epping et al. [33], the volume of the microporosity can be calculated using the following expression:

$$\varnothing^{\mathrm{EDL}} = A_{\mathrm{min}} D_L \tag{9}$$

where A_{min} is the charged surface area of the mineral. The Debye length, D_L, is the distance from the charged surface to the point where electrical potential decays by a factor of e and can be described as follows:

$$D_L = \frac{\beta_D}{\sqrt{I}} \tag{10}$$

where β_D is a temperature dependent factor (2.15×10^{-10} at 25 °C) and I is the ionic strength of the free water. The Debye length is a function of temperature and the ionic strength of the free water in the macroporosity [33].

3 Conceptual model of biogeochemical processes and reaction network in LCdA sediments

An illustration of the conceptual framework is shown in Fig. 1. Sengor et al. [11] developed a 1-D quantitative model to evaluate the fate and transport of heavy metals (i.e., Zn, Pb, and Cu) in LCdA sediments, initially sorbed onto Fe hydroxides [11]. The model focused on the competing effects of heavy metal mobilization through reductive dissolution of Fe hydroxides by Fe-reducing bacteria (FRB) and precipitation at depth as metal sulfides due to biogenic sulfide formation by sulfate reducing bacteria (SRB). The results showed that the relative rates of FRB and SRB were a key factor controlling the mobilization of heavy metals and pH within the sediment depth. The study demonstrated inorganic diffusive transport model coupled to a biotic reaction network including biodegradation kinetics with multiple terminal electron acceptors and biotransformation dynamics of redox front. The reader is referred to Sengor et al. [11] for details of the solid phase and pore water chemistry, available sediment, and water sample data that formed the basis of the conceptual model. Table 1 details the geochemical reaction network and corresponding kinetic rate law expressions used in the model [11]. Microbially mediated reaction network and corresponding kinetic expressions are given in Table 2. The initial concentrations used in the model are provided in Table 3. Parameter values for the kinetic rate constants used in the biogeochemical model are listed in Table 4. The aqueous complexation reactions along with log K constants are listed in Table 5.

The diffusive reactive transport model presented by Sengor et al. [11] used a uniform diffusion coefficient for all species (4.27×10^{-6} cm^2/s) using Fickian diffusion, based on an average diffusion coefficient value calculated after Balistrieri [36]. In this study, the role of Nernst-Planck representation of diffusion (e.g., MCD modeling) on the overall effluent composition is investigated using effective diffusion coefficients based on Eq. (5), where the species-specific diffusion coefficients are obtained from Table 6 given below. The porosity is taken to be 0.77, based on an average value reported by Balistrieri [36]. The EDL effects are implemented in this study involving the species-specific diffusion according to Table 6 and an EDL that compensates the surface charge of Fe hydroxide (i.e., ferrihydrite). Based on the ionic strength of

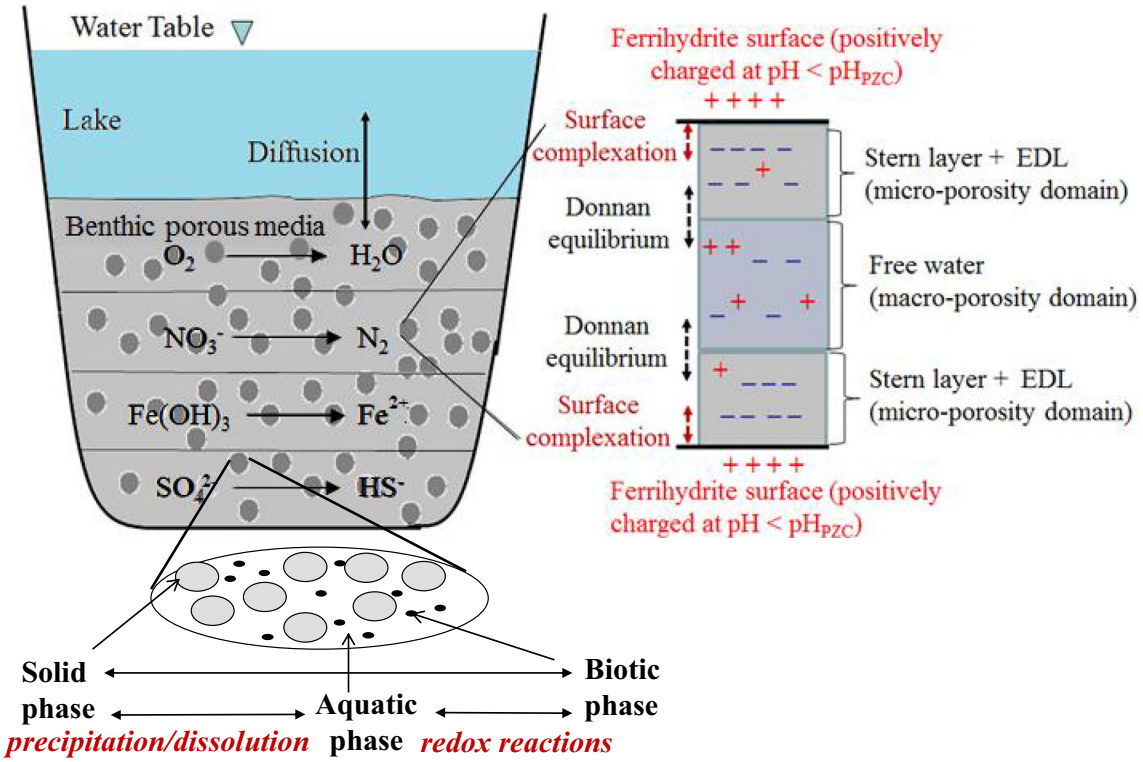

Fig. 1 Illustration of the benthic porous media with primary processes governing the fate and transport of trace metals

porewater composition (0.0035 M), the Debye length of the EDL can be calculated from Eq. (10) as 5.07×10^{-9} m. From the surface area of ferrihydrite (205 m^2/g as discussed by Sengor et al. [11]) and Debye length of 5.07×10^{-9} m, the microporosity of the EDL would be 5% using Eq. (9). The chemical and microbial reaction networks based on Sengor et al. [11] are shown in Tables 1, 2, 3, and 4.

4 Results and discussion

The present study aims at the investigation of species-specific multicomponent diffusion (i.e., Nernst-Planck representation of diffusion using Table 6, versus the uniform Fickian diffusion of species in the sediments) and the explicit treatment of electrostatic effects, on the overall dynamics of biogeochemical cycling of heavy metals in the system. The solute benthic fluxes at the LCdA sediments are controlled by diffusion. Based on this observation, the biogeochemical model is focused purely on diffusive transport. In such systems, the electrochemical potential of species in the system can play an important role, which would thus impact the overall biogeochemical processes. In this study, the conceptual model and chemical and microbial reaction network are based on the previously published work without any modifications. Although a visual comparison of available field data with new model predictions is made, any re-calibration of the model to fit field data is not considered.

The model results are presented as computed concentrations as a function of sediment depth corresponding to simu-

Table 1 Geochemical reaction network and corresponding kinetic rate law expressions used in the model (from [11])

Ferrihydrite	$Fe(OH)_3 + 3H^+ \rightleftharpoons Fe^{3+} + 3H_2O$	Equilibrium
Mackinawite	$FeS + H^+ \rightleftharpoons Fe^{2+} + HS^-$	Equilibrium
Siderite	$FeCO_3 \rightleftharpoons Fe^{2+} + CO_3^{2-}$	$R_{FeCO_3} = 1 \times 10^{-12} \frac{SI_{FeCO3}}{\lvert SI_{FeCO3} \rvert + 0.5}$
Sphalerite	$ZnS + H^+ \rightleftharpoons Zn^{2+} + HS^-$	$R_{ZnS} = 1 \times 10^{6} [Zn^{2+}][H_2S] \frac{SI_{ZnS}}{\lvert SI_{ZnS} \rvert + 0.5}$
Galena	$PbS + H^+ \rightleftharpoons Pb^{2+} + HS^-$	$R_{PbS} = 1 \times 10^{6} [Pb^{2+}][H_2S] \frac{SI_{PbS}}{\lvert SI_{PbS} \rvert + 0.5}$
Chalcocite	$Cu_2S + H^+ \rightleftharpoons 2Cu^+ + HS^-$	$R_{Cu_2S} = 1 \times 10^{14} [Cu^+]^2 [H_2S] \frac{SI_{Cu_2S}}{\lvert SI_{Cu_2S} \rvert + 0.5}$

SI is the mineral saturation index, log (Q/K), where Q and K represent the activity product and equilibrium constant for the reaction shown, respectively

Table 2 Microbially mediated reactions and corresponding kinetic rate expressions (from [11])

Microbially mediated reactions

$CH_3COO^- + 2O_2 \rightleftharpoons 2CO_3^{2-} + 3H^+$	R_{O_2}	$\log K = 126.09$
$CH_3COO^- + 1.6NO_3^- \rightleftharpoons 2CO_3^{2-} + 0.8N_2 + 1.4H^+ + 0.8H_2O$	$R_{NO_3^-}$	$\log K = 153.6$
$CH_3COO^- + 8Fe^{3+} + 4H_2O \rightleftharpoons 8Fe^{2+} + 2CO_3^{2-} + 11H^+$	$R_{Fe^{3+}}$	$\log K = 58.17$
$CH_3COO^- + SO_4^{2-} \rightleftharpoons 2CO_3^{2-} + HS^- + 2H^+$	$R_{SO_4^{2-}}$	$\log K = -12.23$

Kinetic rate laws

$$R_{O_2} = V_m^{O_2} \frac{[O_2]}{[O_2]+K_s^{O_2}} \frac{\log\left(Q_{O_2}/K_{O_2}\right)}{\log\left(Q_{O_2}/K_{O_2}\right)+0.5}$$

$$R_{NO_3^-} = V_m^{NO_3^-} \frac{\left[NO_3^-\right]}{\left[NO_3^-\right]+K_s^{NO_3^-}} \frac{K_{O_2}^{in}}{K_{O_2}^{in}+[O_2]} \frac{\log\left(Q_{NO_3^-}/K_{NO_3^-}\right)}{\log\left(Q_{NO_3^-}/K_{NO_3^-}\right)+0.5}$$

$$R_{Fe^{3+}} = V_m^{Fe^{3+}} \frac{K_{O_2}^{in}}{K_{O_2}^{in}+[O_2]} \frac{K_{NO_3^-}^{in}}{K_{NO_3^-}^{in}+[NO_3]} \frac{\log\left(Q_{Fe^{3+}}/K_{Fe^{3+}}\right)}{\log\left(Q_{Fe^{3+}}/K_{Fe^{3+}}\right)+0.5}$$

$$R_{SO_4^{2-}} = V_m^{SO_4^{2-}} \frac{\left[SO_4^{-2}\right]}{\left[SO_4^{-2}\right]+K_s^{SO_4^{2-}}} \frac{K_{O_2}^{in}}{K_{O_2}^{in}+[O_2]} \frac{K_{NO_3^-}^{in}}{K_{NO_3^-}^{in}+\left[NO_3^-\right]} \frac{K_{Fe^{3+}}^{in}}{K_{Fe^{3+}}^{in}+\left[Fe^{+3}\right]} \frac{\log\left(Q_{SO_4^{2-}}/K_{SO_4^{2-}}\right)}{\log\left(Q_{SO_4^{2-}}/K_{SO_4^{2-}}\right)+0.5}$$

$V_m^{\ i}$ maximum substrate utilization rate constant using the ith terminal electron acceptor (TEA), $K_s^{\ i}$ half saturation constant for the ith TEA, K_i^{in} inhibition constants due the ith TEA, Q_i, K_i activity product and equilibrium constant for the corresponding TEA utilizing reaction

lated time periods of 5 years, representing the time after which near steady-state conditions are observed (using the microbial reaction rates in Table 4). The sediment depth of 40 cm in the model results is based on a representative depth to capture the redox disequilibrium conditions and calculated concentration trends of main species during the transition from suboxic to anoxic conditions within the sediment.

Table 3 Initial concentrations used in the model (from [11])

Aqueous species	Units	Value
pH		7.2
Total inorganic carbon	M	3.535×10^{-4}
Ca^{2+}	M	1.372×10^{-4}
Mg^{2+}	M	8.641×10^{-5}
Fe^{2+}	M	2.034×10^{-19} (≈ 0)
Fe^{3+}	M	3.009×10^{-9}
K^+	M	1.279×10^{-5}
S^{2-}	M	1.3093×10^{-142} (≈ 0)
SO_4^{-2}	M	5.830×10^{-5}
Na^+	M	1.000×10^{-4}
Cl^-	M	1.946×10^{-5}
$O_{2(aq)}$	M	2.700×10^{-4} [a]
NO_3^-	M	1.800×10^{-5} [a]
$N_{2(aq)}$	M	9.150×10^{-19} (≈ 0)
Pb^{2+}	M	5.309×10^{-8}
Cu^+	M	1.180×10^{-8}
Zn^{2+}	M	8.717×10^{-6}
$Acetate^-$	M	7.000×10^{-3}
Br^-	M	1.00×10^{-30} (≈ 0)

[a] Based on the saturation of O_2 under 25 °C and nitrate data from Winowiecki [37]

Table 4 Parameter values for the kinetic constants used in the biogeochemical model (from [11])

Parameter	Units	Value used in the model
$V_m^{O_2}$	s^{-1}	5×10^{-9} [a]
$V_m^{NO_3^-}$	s^{-1}	2×10^{-10} [b]
V_m^{Fe3+}	s^{-1}	3×10^{-12} [c]
$V_m^{SO_4^{2-}}$	s^{-1}	3×10^{-9} [c]
$K_s^{O_2}$	M	2.41×10^{-5} [d]
$K_s^{NO_3^-}$	M	1.13×10^{-4} [d]
$K_s^{SO_4^{2-}}$	M	1×10^{-3} [e]
$K_{O_2}^{in}$	M	1.61×10^{-8} [d]
$K_{NO_3^-}^{in}$	M	1×10^{-7} [c]
$K_{Fe^{3+}}^{in}$	M	1×10^{-8} [c]

[a] Estimated from Russell [38]

[b] Estimated from Parkhurst and Appelo [39]

[c] Sengor et al. [11]

[d] Estimated from Doussan et al. [40]

[e] Estimated from Brugato [41]

Table 5 Aqueous complexation reactions used in the biogeochemical model (from [42])

Reaction	Log K (25 °C)
$S^{2-} + H^+ \rightleftharpoons HS^-$	17.300
$OH^- + H^+ \rightleftharpoons H_2O$	13.997
$PbOH^+ + H^+ \rightleftharpoons Pb^{2+} + H_2O$	7.597
$Pb(OH)_{2(aq)} + 2H^+ \rightleftharpoons Pb^{2+} + 2H_2O$	17.094
$Pb(OH)_3^- + 3H^+ \rightleftharpoons Pb^{2+} + 3H_2O$	28.091
$Pb_2OH^{3+} + H^+ \rightleftharpoons 2Pb^{2+} + H_2O$	6.397
$Pb_3(OH)_4^{2+} + 4H^+ \rightleftharpoons 3Pb^{2+} + 4H_2O$	23.888
$Pb(OH)_4^{2-} + 4H^+ \rightleftharpoons Pb^{2+} + 4H_2O$	39.699
$Pb_4(OH)_4^{4+} + 4H^+ \rightleftharpoons Pb^{2+} + 4H_2O$	19.988
$ZnOH^+ + H^+ \rightleftharpoons Zn^{2+} + H_2O$	8.9970
$Zn(OH)_{2(aq)} \rightleftharpoons Zn^{2+} + 2H_2O - 2H^+$	17.794
$Zn(OH)_3^- + 3H^+ \rightleftharpoons Zn^{2+} + 3H_2O$	28.091
$Zn(OH)_4^{2-} + 4H^+ \rightleftharpoons Zn^{2+} + 4H_2O$	40.488
$FeOH^+ + H^+ \rightleftharpoons Fe^{2+} + H_2O$	9.397
$Fe(OH)_{2(aq)} + 2H^+ \rightleftharpoons Fe^{2+} + 2H_2O$	20.494
$Fe(OH)_3^- + 3H^+ \rightleftharpoons Fe^{2+} + 3H_2O$	28.991
$FeOH^{2+} + H^+ \rightleftharpoons Fe^{3+} + H_2O$	2.187
$Fe(OH)_2^+ + 2H^+ \rightleftharpoons Fe^{3+} + 2H_2O$	4.594
$Fe(OH)_{3(aq)} + 3H^+ \rightleftharpoons Fe^{2+} + 3H_2O$	12.560
$Fe(OH)_4^- + 4H^+ \rightleftharpoons Fe^{3+} + 4H_2O$	21.588
$Fe_2(OH)_2^{4+} + 2H^+ \rightleftharpoons 2Fe^{3+} + 2H_2O$	2.854
$Fe_3(OH)_4^{5+} + 4H^+ \rightleftharpoons 3Fe^{3+} + 4H_2O$	6.288
$MgOH^+ + H^+ \rightleftharpoons Mg^{2+} + H_2O$	11.397
$CaOH^+ + H^+ \rightleftharpoons Ca^{2+} + H_2O$	12.697
$PbCl^+ \rightleftharpoons Pb^{2+} + Cl^-$	− 1.550
$PbCl_{2(aq)} \rightleftharpoons Pb^{2+} + 2Cl^-$	− 2.200
$PbCl_3^- \rightleftharpoons Pb^{2+} + 3Cl^-$	− 1.800
$PbCl_4^{2-} \rightleftharpoons Pb^{2+} + 4Cl^-$	− 1.460
$ZnCl^+ \rightleftharpoons Zn^{2-} + Cl^-$	− 0.400
$ZnCl_{2(aq)} \rightleftharpoons Zn^{2+} + 2Cl^-$	− 0.600
$ZnCl_3^- \rightleftharpoons Zn^{2+} + 3Cl^-$	− 0.500
$ZnCl_4^{2-} \rightleftharpoons Zn^{2+} + 4Cl^-$	− 0.199
$ZnOHCl_{(aq)} + H^+ \rightleftharpoons Zn^{2+} + Cl^- + H_2O$	7.480
$FeCl^{2+} \rightleftharpoons Fe^{3+} + Cl^-$	− 1.480
$FeCl_2^+ \rightleftharpoons Fe^{3+} + 2Cl^-$	− 2.130
$FeCl_{3(aq)} \rightleftharpoons Fe^{3+} + 3Cl^-$	− 1.130
$H_2S_{(aq)} \rightleftharpoons H^+ + HS^-$	− 7.020
$Pb(HS)_{2(aq)} \rightleftharpoons Pb^{2+} + 2HS^-$	− 14.710
$Pb(HS)_3^- \rightleftharpoons Pb^{2+} + 3HS^-$	− 16.001
$ZnS(HS)_2^{2-} + H^+ \rightleftharpoons Zn^{2+} + 3HS^-$	− 6.120
$Zn(HS)_4^{2-} \rightleftharpoons Zn^{2+} + 4HS^-$	− 14.640
$ZnS(HS)^- + H^+ \rightleftharpoons Zn^{2+} + 2HS^-$	− 6.810
$HSO_4^- \rightleftharpoons H^+ + SO_4^{2-}$	− 1.990
$PbSO_{4(aq)} \rightleftharpoons Pb^{2+} + SO_4^{2-}$	− 2.690
$Pb(SO_4)_2^{2-} \rightleftharpoons Pb^{2+} + 2SO_4^{2-}$	− 3.470
$ZnSO_{4(aq)} \rightleftharpoons Zn^{2+} + SO_4^{2-}$	− 2.340
$Zn(SO_4)_2^{2-} \rightleftharpoons Zn^{2+} + 2SO_4^{2-}$	− 3.280
$FeS_{(aq)} \rightleftharpoons Fe^{2+} + HS^-$	2.200
$FeSO_{4(aq)} \rightleftharpoons Fe^{2+} + SO_4^{2-}$	− 2.390
$FeSO_4^+ \rightleftharpoons Fe^{3+} + SO_4^{2-}$	− 4.050
$Fe(SO_4)_2^- \rightleftharpoons Fe^{2+} + 2SO_4^{2-}$	− 5.380
$MgSO_{4(aq)} \rightleftharpoons Mg^{2+} + SO_4^{2-}$	− 2.260
$CaSO_{4(aq)} \rightleftharpoons Ca^{2+} + SO_4^{2-}$	− 2.360
$NaSO_4^- \rightleftharpoons Na^+ + SO_4^{2-}$	− 0.730
$KSO_4^- \rightleftharpoons K^+ + SO_4^{2-}$	− 0.850
$PbNO_3^+ \rightleftharpoons Pb^{2+} + NO_3^-$	− 1.170
$Pb(NO_3)_{2(aq)} \rightleftharpoons Pb^{2+} + 2NO_3^-$	− 1.400
$ZnNO_3^- \rightleftharpoons Zn^{+2} + NO_3^-$	− 0.400
$Zn(NO_3)_{2(aq)} \rightleftharpoons Zn^{2+} + 2NO_3^-$	0.300
$FeNO_3^{2+} \rightleftharpoons Fe^{3+} + NO_3^-$	− 1.000
$CaNO_3^- \rightleftharpoons Ca^{2-} + NO_3^-$	− 0.500
$HCO_3^- \rightleftharpoons H^+ + CO_3^{2-}$	− 10.329
$H_2CO_{3(aq)} \rightleftharpoons 2H^+ + CO_3^{2-}$	− 16.681
$Pb(CO_3)_2^{2-} \rightleftharpoons Pb^{2+} + 2CO_3^{2-}$	− 9.938
$PbCO_{3(aq)} \rightleftharpoons Pb^{2+} + CO_3^{2-}$	− 6.478
$PbHCO_3^+ \rightleftharpoons Pb^{2+} + CO_3^{2-} + H^+$	− 13.200
$ZnCO_{3(aq)} \rightleftharpoons Zn^{2+} + CO_3^{2-}$	− 4.760
$ZnHCO_3^+ \rightleftharpoons Zn^{2+} + CO_3^{2-} + H^+$	− 11.829
$FeHCO_3^+ \rightleftharpoons Fe^{+2} + CO_3^{2-} + H^+$	− 11.429
$MgCO_{3(aq)} \rightleftharpoons Mg^{2+} + CO_3^{2-}$	− 2.920
$MgHCO_3^+ \rightleftharpoons Mg^{2+} + CO_3^{2+} + H^+$	− 11.339
$CaHCO_3^- \rightleftharpoons Ca^{2+} + CO_3^{2-} + H^+$	− 11.599
$CaCO_{3(aq)} \rightleftharpoons Ca^{2+} + CO_3^{2-}$	− 3.200
$NaCO_3^- \rightleftharpoons Na^+ + CO_3^{2-}$	− 1.270
$NaHCO_{3(aq)} \rightleftharpoons Na^+ + CO_3^{2-} + H^+$	− 10.079
$H(Acetate)_{(aq)} \rightleftharpoons Acetate^- + H^+$	− 4.757
$Pb(Acetate)^+ \rightleftharpoons Acetate^- + Pb^{2+}$	− 2.680
$Pb(Acetate)_{2(aq)} \rightleftharpoons 2Acetate^- + Pb^{2+}$	− 4.080
$Zn(Acetate)^+ \rightleftharpoons Acetate^- + Zn^{2+}$	− 1.580
$Zn(Acetate)_{2(aq)} \rightleftharpoons 2Acetate^- + Zn^{2+}$	− 2.643
$Fe(Acetate)^+ \rightleftharpoons Acetate^- + Fe^{2+}$	− 1.400
$Fe(Acetate)^{2+} \rightleftharpoons Acetate^- + Fe^{3+}$	− 4.023
$Fe(Acetate)_2^+ \rightleftharpoons 2Acetate^- + Fe^{3+}$	− 7.572
$Fe(Acetate)_{3(aq)} \rightleftharpoons 3Acetate^- + Fe^{3+}$	− 9.587
$Mg(Acetate)^+ \rightleftharpoons Acetate^- + Mg^{2+}$	− 1.270
$Ca(Acetate)^+ \rightleftharpoons Acetate^- + Ca^{2+}$	− 1.180
$Na(Acetate)_{(aq)} \rightleftharpoons Acetate^- + Na^+$	0.180
$K(Acetate)_{(aq)} \rightleftharpoons Acetate^- + K^+$	0.195

4.1 Implementation of MCD modeling

Comparative simulation results for various anions and cations involved in the reactive transport model are given in Figs. 2, 3, 5, and 6. Computed amounts of precipitating minerals with

Table 6 Diffusion coefficients of aqueous species used in the MCD model [43]

Aqueous species	Diffusion coefficient ($\times 10^{-10}$ m^2/s)
$Acetate^-$	12.10
Ca^{2+}	7.92
Cl^-	20.30
CO_3^{2-}	9.20
Cu^+	15.10
Fe^{2+}	7.19
Fe^{3+}	6.04
H^+	93.10
HCO_3^-	11.90
HS^-	17.30
K^+	19.60
Mg^{2+}	7.06
Mn^{2+}	7.12
N_2	18.80
Na^+	13.30
NH_4^+	19.60
NO_3^-	19.00
O_2	21.00
SO_4^{2-}	10.70
Pb^{2+}	9.45
Zn^{2+}	7.03

depth are shown in Fig. 4. Assessing the difference between single uniform diffusion (i.e., Fickian) versus species-specific diffusion (i.e., MCD with Nernst-Planck representation) shows significant differences in the profile of almost all species. While in the case of a single uniform diffusion coefficient the profile of species is dependent on the magnitude of the diffusion coefficient and the concentration gradient of the species across the column, in the case of species-specific diffusion the profile of species is a function of the diffusion coefficient of the species itself as well as the diffusion coefficients of other charged ions, the magnitude and direction of concentration gradients of all species in the system, and the concentration of that species in solution.

The simulation of a conservative tracer (Br) provides the comparison of non-reactive versus reactive (the rest of other ions) species transport in response to the MCD implementation. The results for the conservative tracer (Br) in Fig. 3 (above panel) predict the flushing of the column (initial concentration is 0) with a hypothetical 1×10^{-6} M concentration, as there has not been any field data reported on tracer concentrations. The model results show a faster decrease of the tracer with depth in the presence of MCD, which is due to the higher diffusion coefficient of the tracer, compared to the uniform diffusion coefficient value used for all ions.

The model results of heavy metals (Pb and Zn) (as given in Figs. 2, 5, and 6), on the other hand, show higher concentration profiles throughout the depth of the column when MCD is implemented in the model, compared to the case of a single uniform diffusion coefficient assumed for all charged species. Especially prior to the suboxic zone (top 5 to 10 cm of the column where before the mobilization of heavy metals by reductive dissolution of ferrihydrite begins), the higher concentrations of Zn and Pb predicted in the porewater are mainly due to the slightly lower pH conditions observed in the system when electrochemical potential of ions is considered in MCD simulations. Thus, the resulting lower pH leads to less adsorption of heavy metals onto the Fe hydroxide surface yielding higher concentrations in the porewater. In addition to this effect, in the anoxic zone (depths below 5–10 cm of the column) the production of biogenic sulfide by SRB results in the formation of aqueous (bi)sulfide complexes, where the majority of the soluble sulfide exists as these aqueous species along with $FeS_{(aq)}$. As reported by Sengor et al. (2007a, b), these soluble complexes play an important role on the overall dynamics of heavy metals. As the heavy metals are solubilized into the porewater due to the microbial reductive dissolution of ferrihydrite by FRB, they tend to form strong metal (bi)sulfide complexes (e.g., Zn-HS; Pb-HS). This further enhances the desorption of heavy metals from the Fe hydroxide surface and competes for the precipitation of Fe and other metal sulfide minerals. The model simulation results show that this competitive effect is more pronounced when the species-specific MCD is considered compared to the uniform species diffusion case. As seen in Figs. 5 and 6, the distribution of sulfide aqueous species results in higher metal (bi)sulfide complexes within the anoxic zone in MCD case, compared to uniform diffusion case predictions. This strong metal (bi)sulfide formation corresponds to the delay of metal sulfide precipitate formation in MCD predictions, whereas relatively lower concentrations of metal (bi)sulfide complexes results in earlier precipitation of metal sulfides in uniform diffusion case (see Fig. 4). The simulation results thus illustrate the importance of biogenic sulfide produced by SRB to be further pronounced when MCD is implemented in reactive transport simulations, impacting the solubility and dynamics of heavy metals in diffusion-dominated systems.

The comparative simulation results in both MCD and uniform diffusion cases can also be compared with the available measured field data compiled from various sources. A visual comparison of available data with model simulations also shows a better match when MCD is implemented in the reactive transport model, especially for dissolved inorganic carbon and partly for Pb and Zn (Fig. 3). The variations in the reported data for various species, especially Pb, Fe, including sulfate, and nitrate yield this visual comparison to be rather less straightforward. However, it should be noted that any recalibration of the model to fit field data is not considered here,

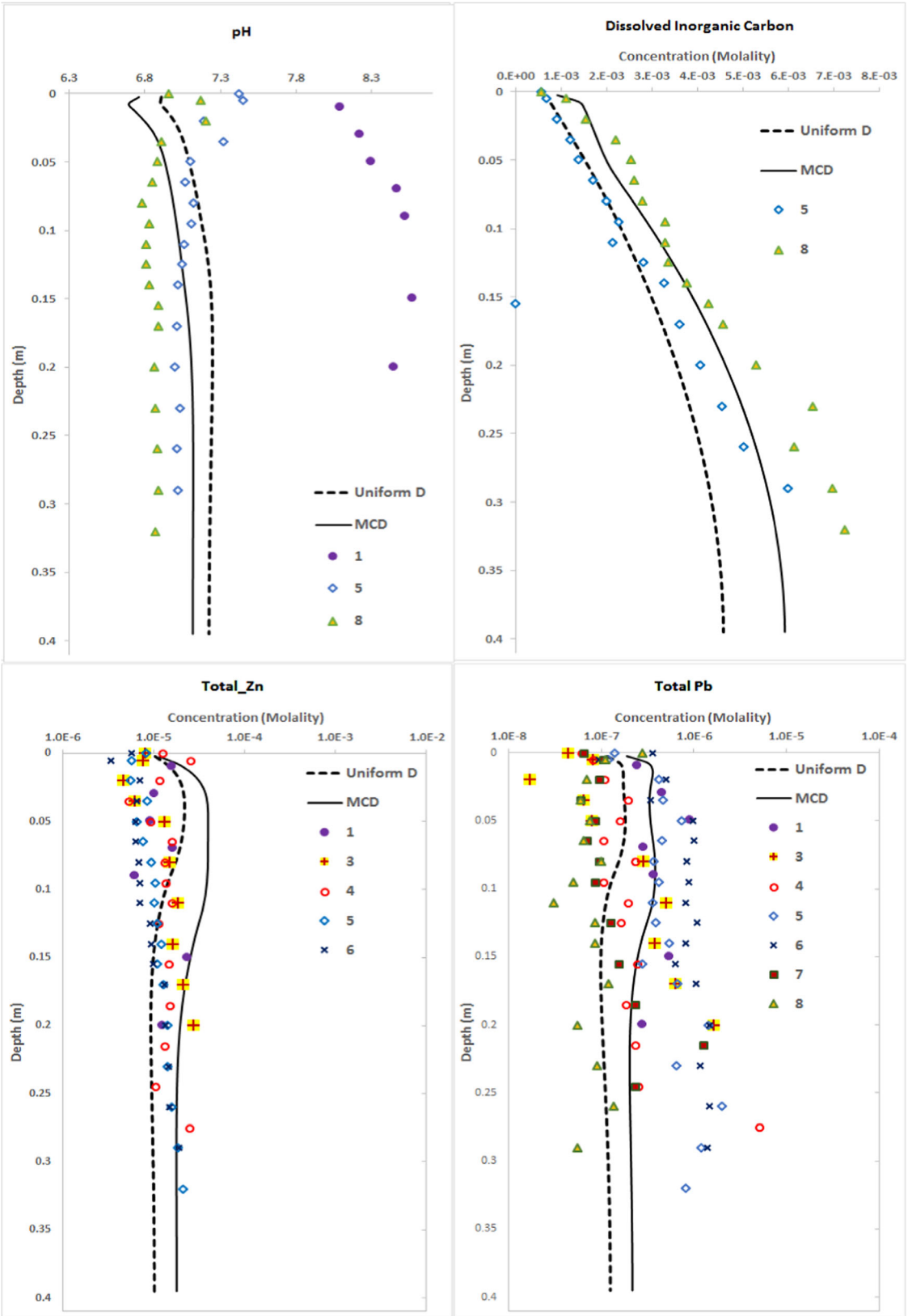

Fig. 2 Comparison of uniform (Fickian) diffusion versus species-dependent MCD (Nernst-Planck) diffusion of main aqueous species (pH, dissolved inorganic carbon, total Pb, and total Zn) as a function of sediment depth. Lines represent model simulations. Symbols show measured data points compiled from various sources (see Sengor et al. [11] for data sources)

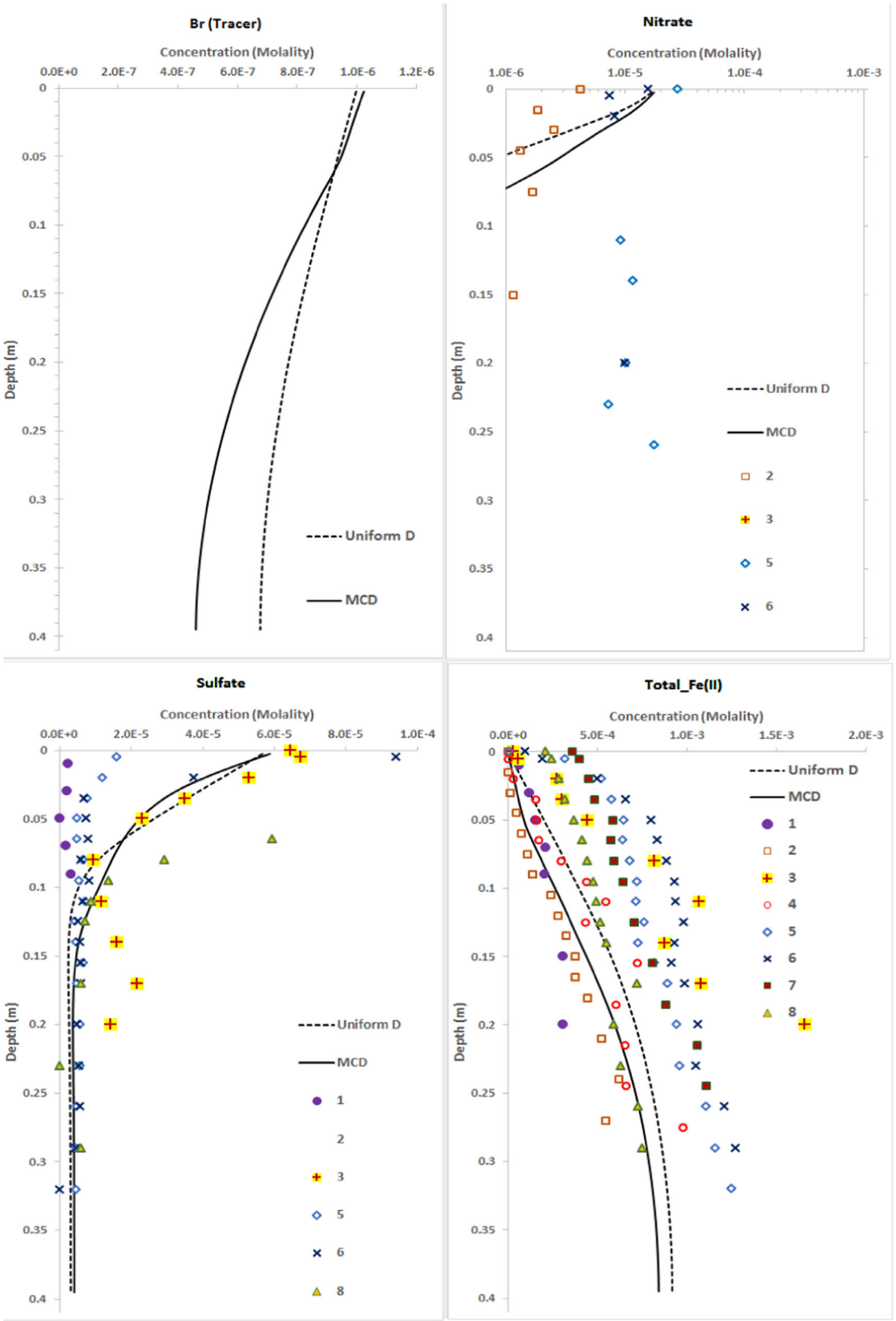

Fig. 3 Comparison of uniform (Fickian) diffusion versus species-dependent MCD (Nernst-Planck) diffusion of main aqueous species (total Br^{-}, NO_3^{-}, SO_4^{-2}, and Fe^{+2}) as a function of sediment depth. Lines represent model simulations. Symbols show measured data points compiled from various sources (see Sengor et al. [11] for data sources)

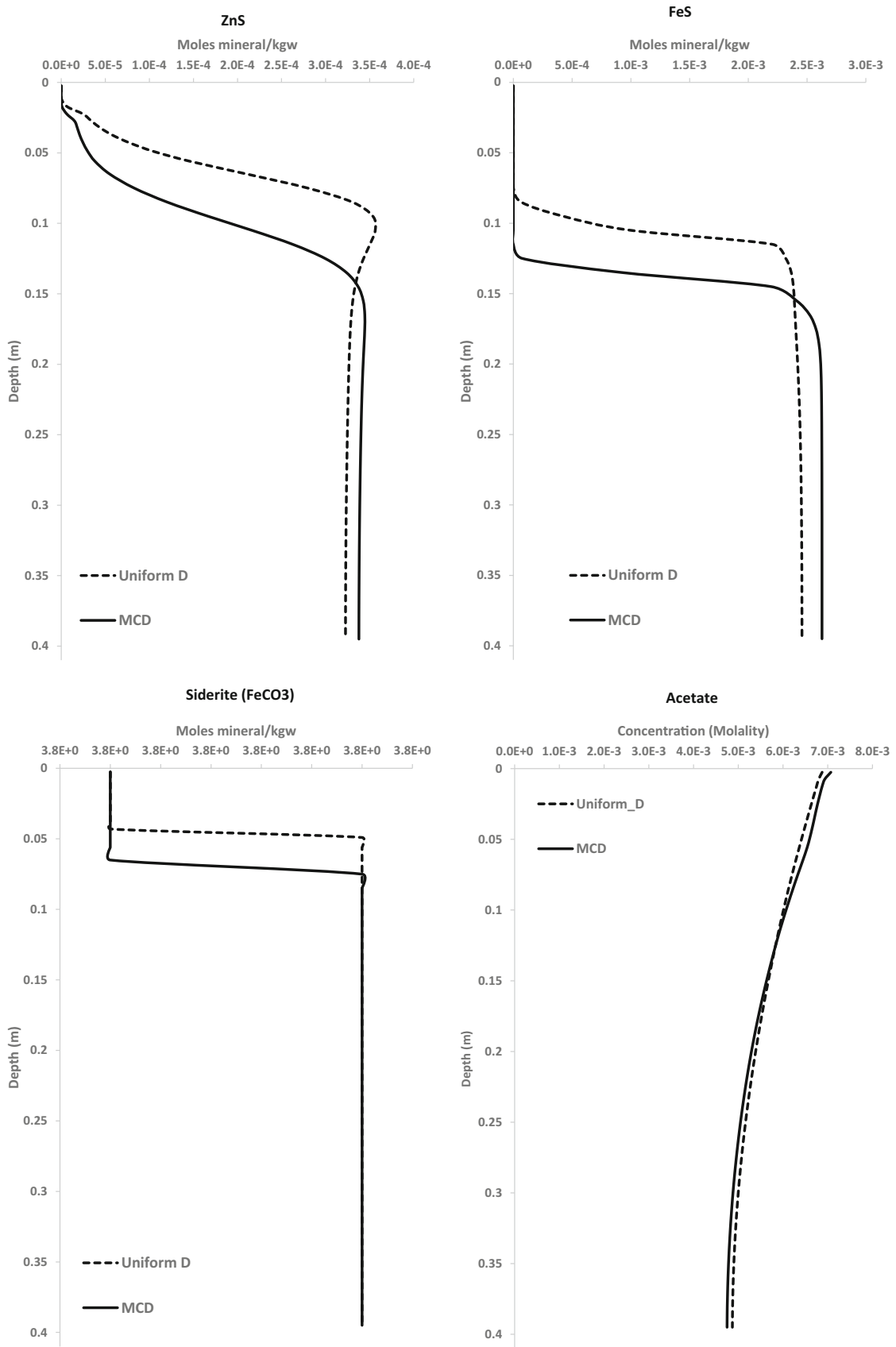

Fig. 4 Computed amounts of precipitating minerals and acetate as a function of depth using uniform (Fickian) diffusion versus species-dependent MCD (Nernst-Planck) diffusion

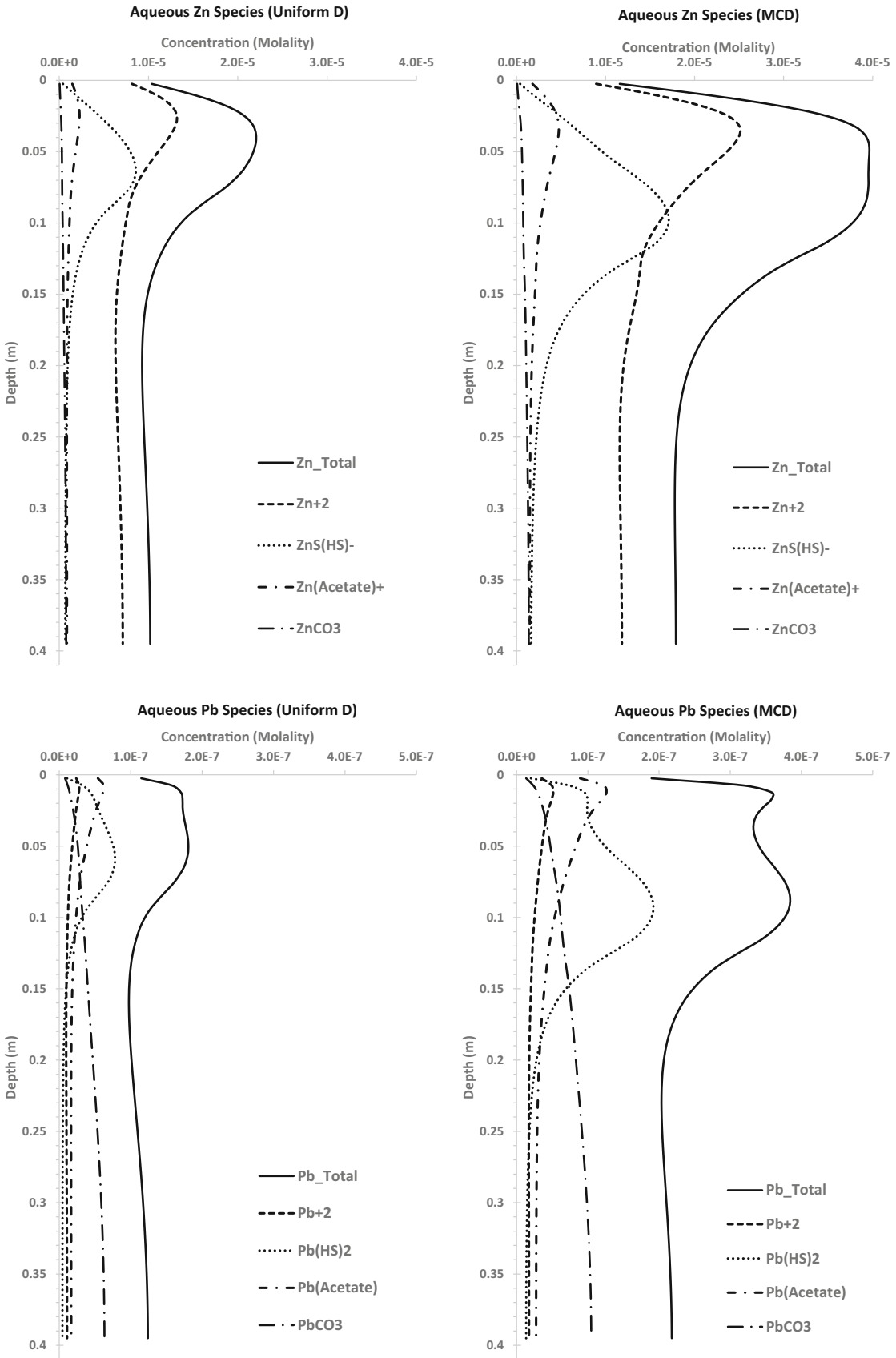

Fig. 5 Calculated distributions of aqueous Zn and Pb species as a function of sediment depth using uniform (Fickian) diffusion (left panel) versus species-dependent MCD (Nernst-Planck) diffusion (right panel)

as this study aims to assess the difference between a Fickian versus Nernst-Planck representation of diffusion on the overall dynamics of heavy metals and biogeochemical processes in purely diffusion controlled environments, such as LCdA sediments, rather than reproducing the measured field data. The results reveal that the use of single uniform diffusion coefficient for all species in purely diffusion-dominated sediments may underestimate the mobility of heavy metals undergoing complex reaction network. The electrochemical potential of species needs to be incorporated in diffusive transport of ions such as the implementation of MCD, for reliable prediction of species transport in such systems.

4.2 Implementation of EDL

The reactive transport modeling of heavy metals in LCdA lake sediments with MCD is also extended to simulate the reactive transport with explicit treatment of electrostatic effects, which involves the implementation of species-specific diffusion according to Table 6 and an EDL that compensates the surface charge of ferrihydrite. As discussed above, this is accomplished by dividing the total pore space in the medium (77%) into two porosity subdomains: (i) microporosity (5% EDL) and (ii) macroporosity (72% free-moving charge-balanced water). Only the water within the macroporosity is assumed to move in response to a gradient. The extent of MCD and EDL effects on the overall biogeochemical processes is investigated by the model results shown for "low" and "high" rates of sulfate and Fe(III) reduction, respectively, considering 5% EDL in all cases. The "low" rates of sulfate reduction are tested as 5 and 3 times lower reduction rates compared to the original rate (i.e., $V_m^{SO_4^{2-}} = 3 \times 10^{-9}\ s^{-1}$), whereas the rates of iron reduction are tested as 2 and 1.5 times higher reduction rates compared to the original rate (i.e., $V_m^{Fe^{3+}} = 3 \times 10^{-12}\ s^{-1}$) given in Table 4. The results are also compared with only MCD implementation case (without EDL effects, i.e., no EDL). The "no EDL" and 5% EDL cases are based on the same original rates of sulfate and iron reduction. The

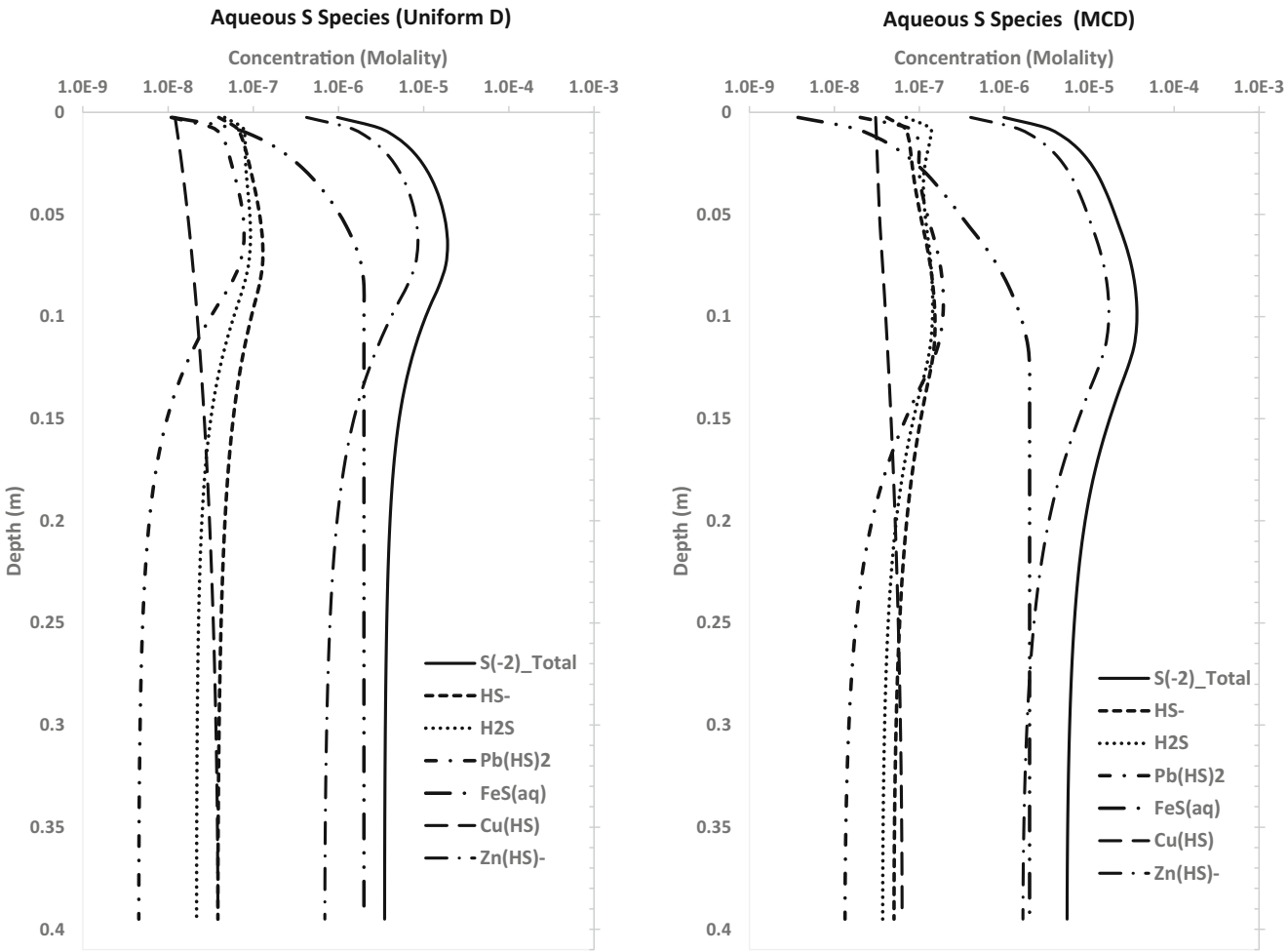

Fig. 6 Calculated distributions of aqueous S species as a function of sediment depth using uniform (Fickian) diffusion (left panel) versus species-dependent MCD (Nernst-Planck) diffusion (right panel)

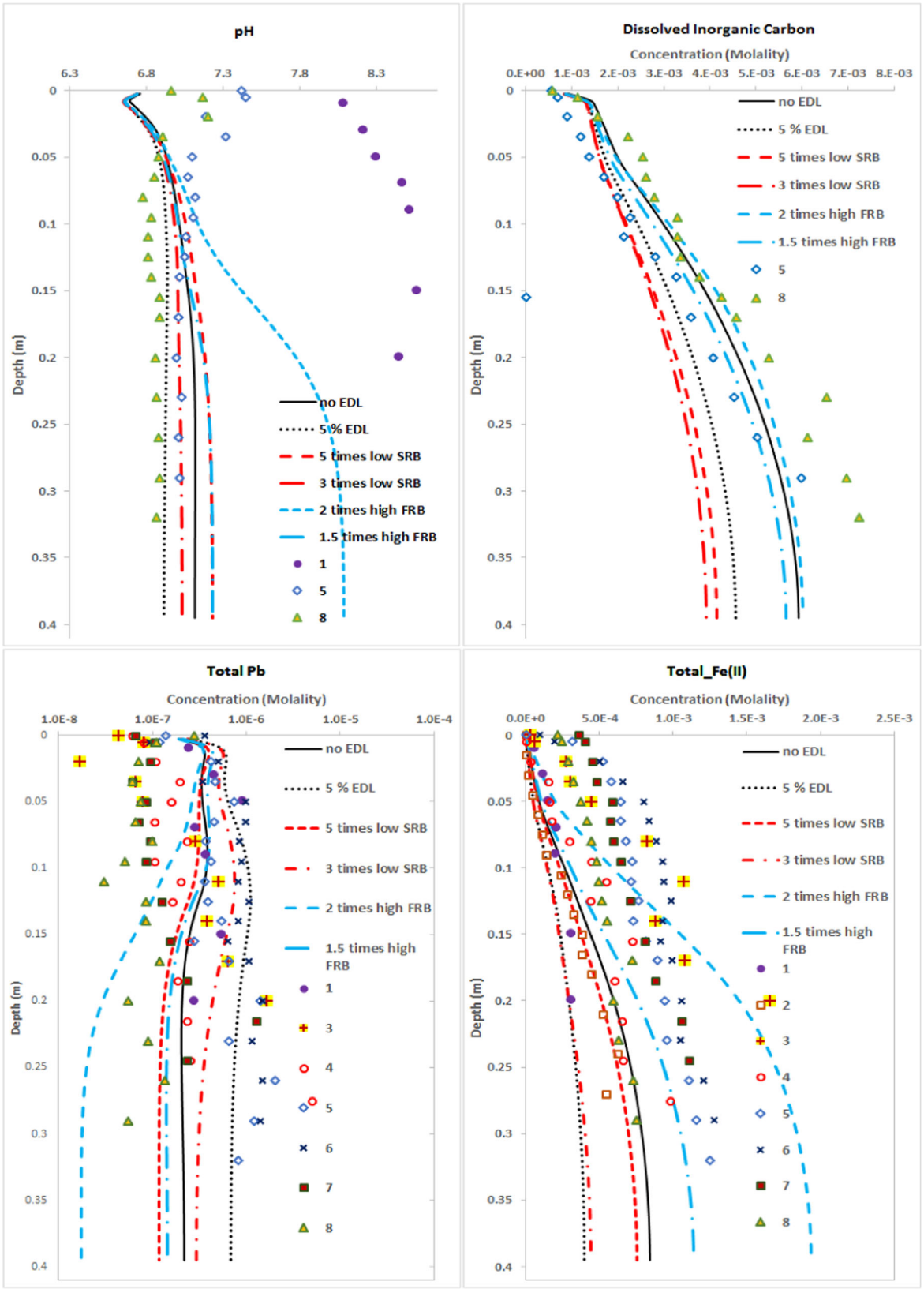

Fig. 7 Computed concentrations of main aqueous species as a function of sediment depth: comparison of model predictions for "low" and "high" rates of SRB (red lines) and FRB (blue lines) activity rates, respectively when 5% EDL is implemented. Symbols show measured data points compiled from various sources (see Sengor et al. [11] for data sources)

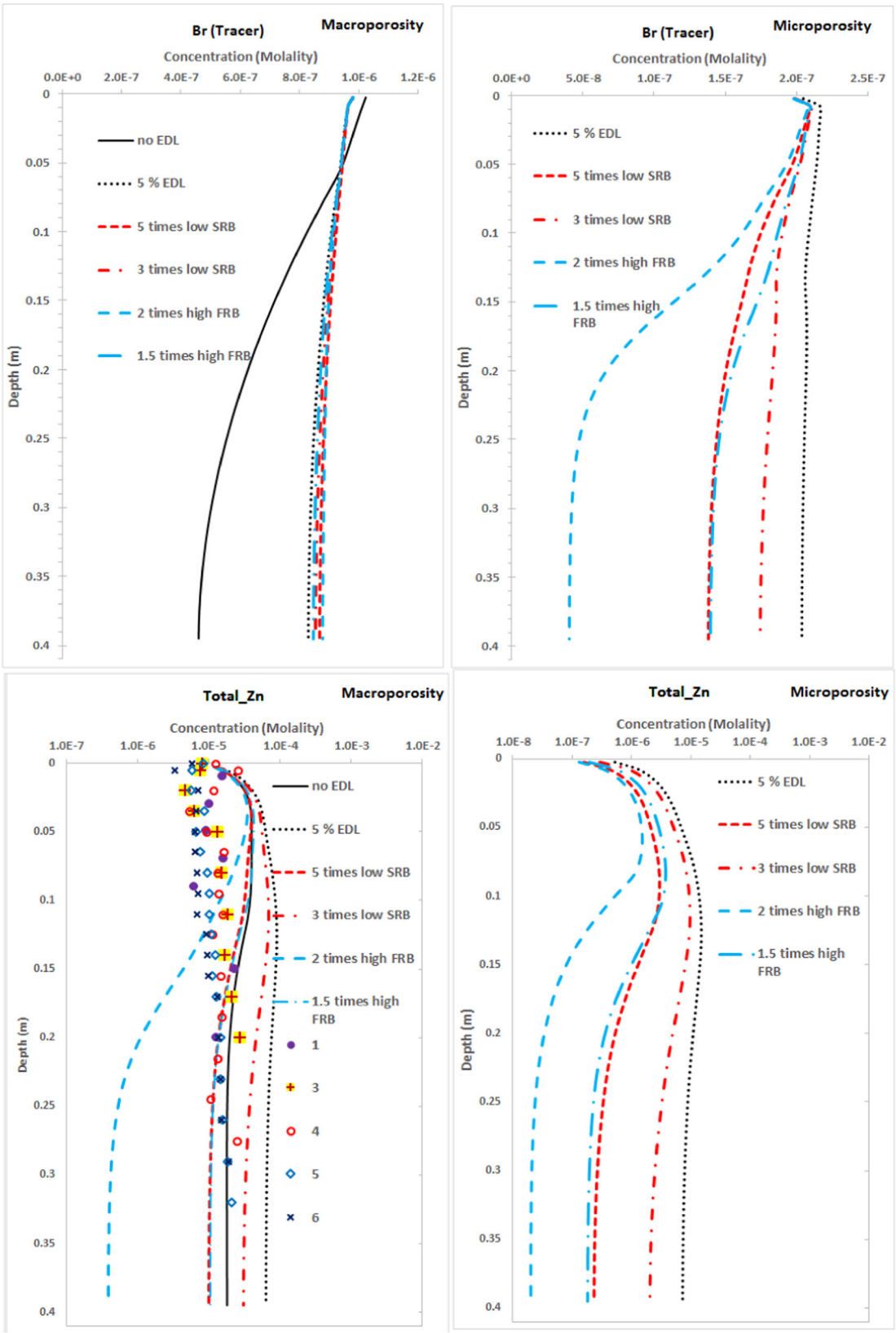

Fig. 8 Computed concentrations of Br (tracer) and total Zn as a function of sediment depth: comparison of model predictions for "low" and "high" rates of SRB (red lines) and FRB (blue lines) activity rates, respectively when 5% EDL is implemented. Symbols show measured data points compiled from various sources (see Sengor et al. [11] for data sources)

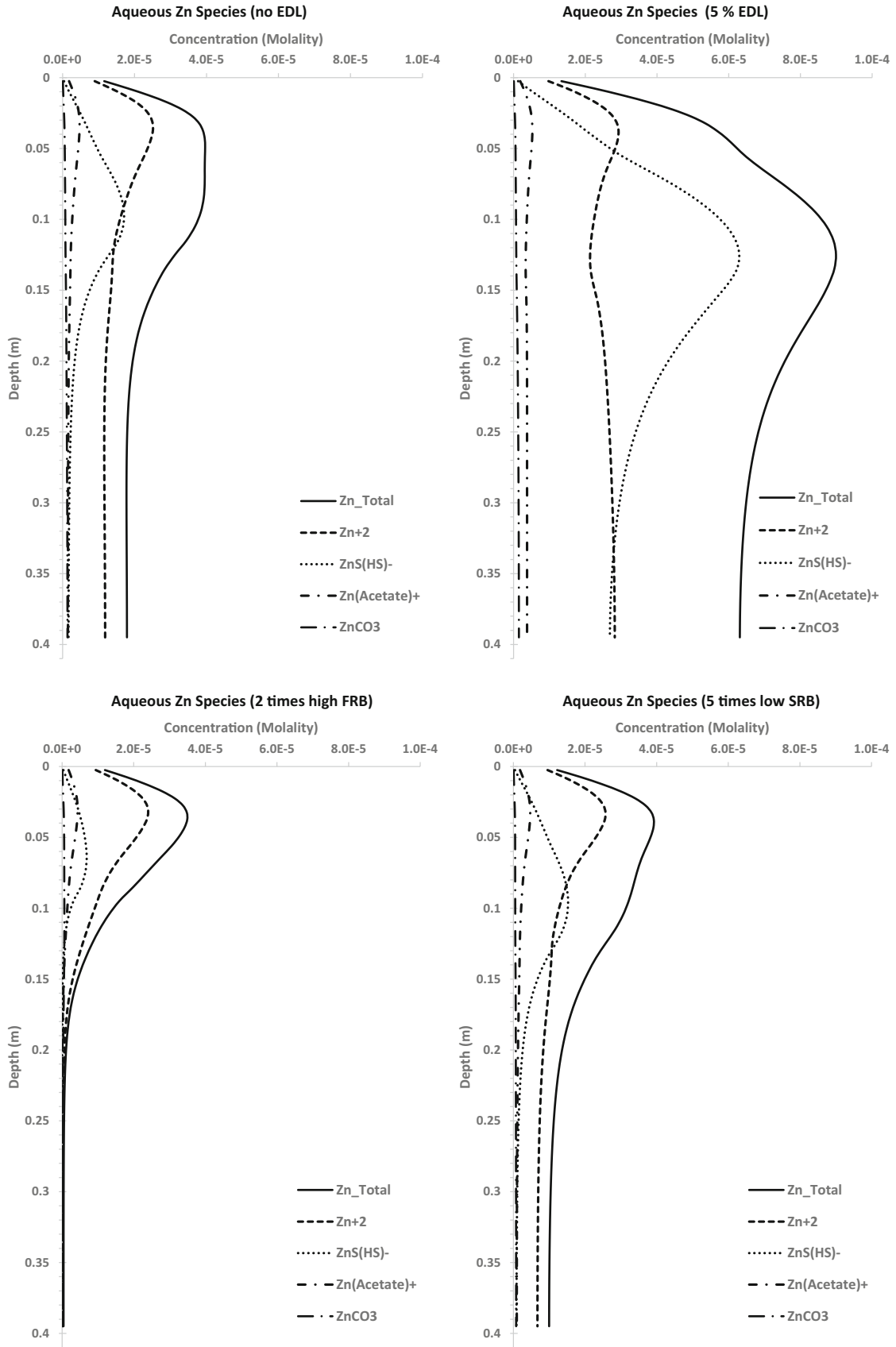

Fig. 9 Calculated distributions of aqueous Zn species as a function of sediment depth: comparison of model predictions for "low" and "high" rates of SRB and FRB activity rates, respectively when 5% EDL is implemented

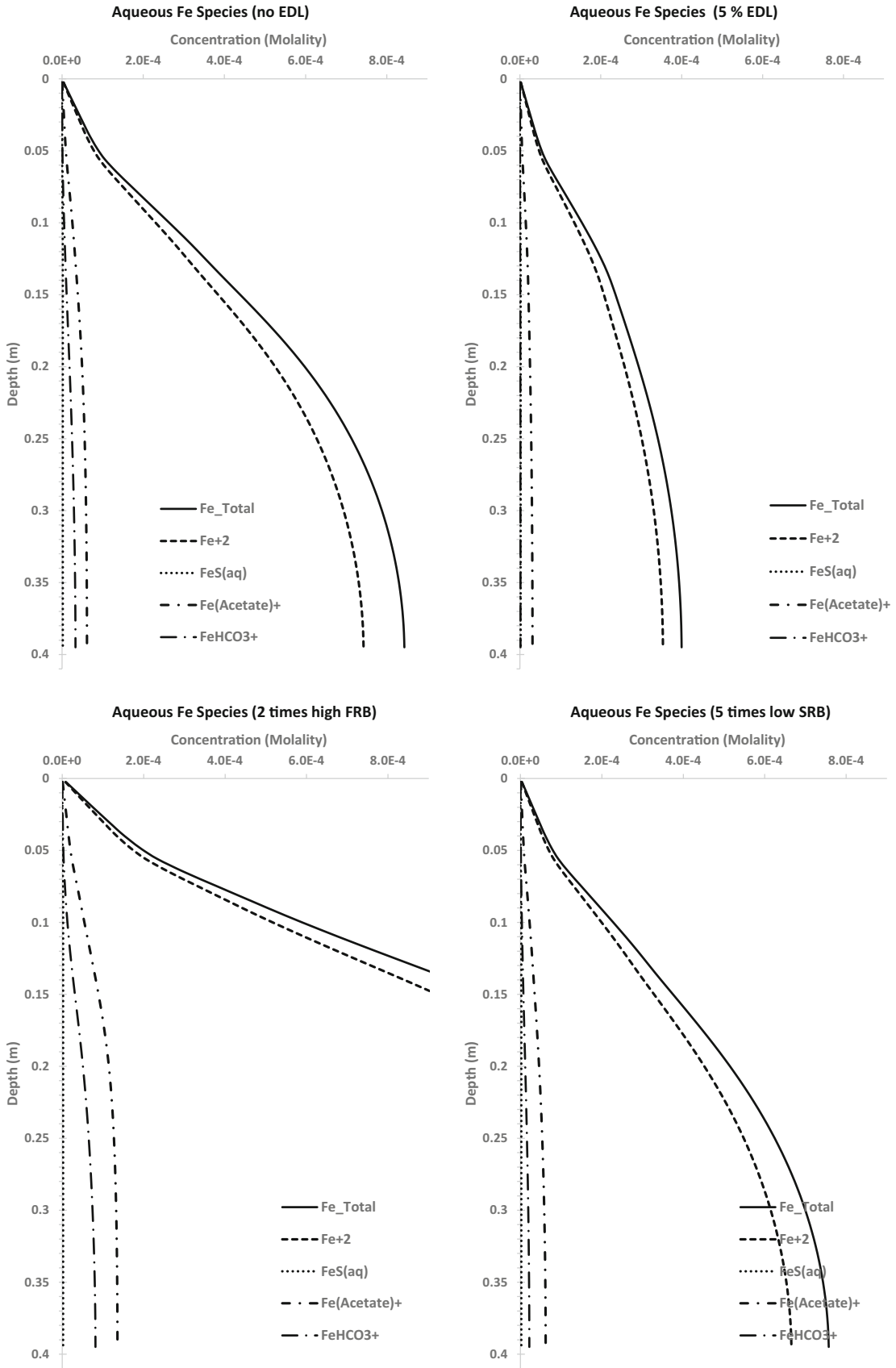

Fig. 10 Calculated distributions of aqueous Fe species as a function of sediment depth: comparison of model predictions for "low" and "high" rates of SRB and FRB activity rates, respectively when 5% EDL is implemented

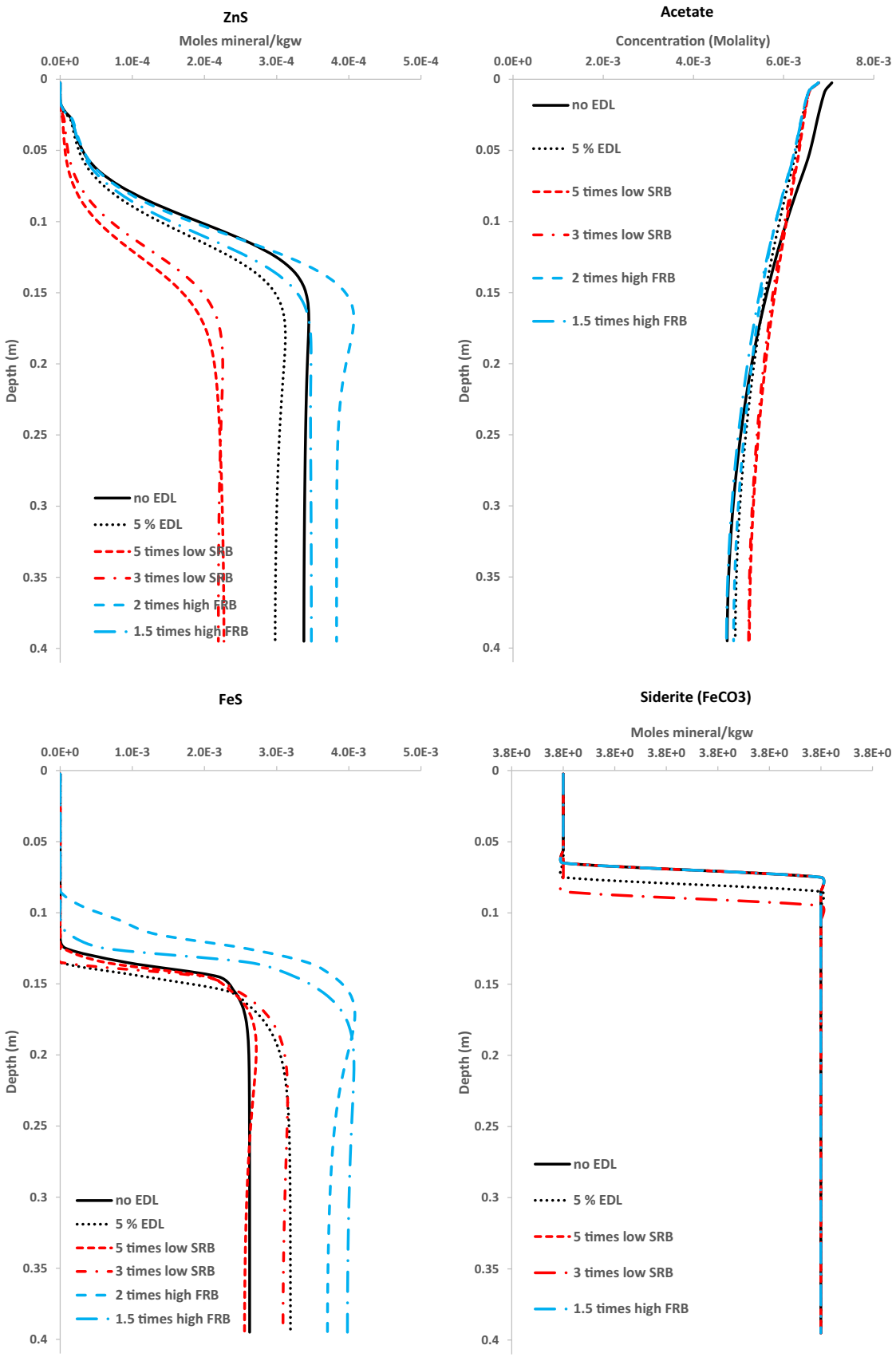

Fig. 11 Computed amounts of precipitating minerals as a function of depth: comparison of model predictions for "low" and "high" rates of SRB (red lines) and FRB (blue lines) activity rates, respectively when 5% EDL is implemented

competitive effects of FRB and SRB activities on pH and overall biogeochemical processes along with MCD and EDL implementation are discussed below.

The comparative simulation results for various anions and cations involved in the reactive transport model are given in Figs. 7, 8, 9, and 10. The "no_EDL" and "5% EDL" simulation results are shown with black lines, whereas the "low" and "high" rates of sulfate and Fe(III) reduction simulations are presented with red and blue lines, respectively. Computed amounts of precipitating minerals with depth are shown in Fig. 11. The results for the conservative tracer (Br) in Fig. 8 show (above left panel) higher concentration of Br to be observed in the free-water domain when EDL is implemented in the code. Due to the positive charge of the ferrihydrite surface below pzc ($pH_{PZC}^{HFO} = 8.11$), Br accumulate at the EDL, and more mass of Br is transferred between the two porosity domains until equilibrium is attained. Therefore, this results in higher concentrations to be retained in the free-water (macroporosity domain). The concentration distribution, however, changes with the change in pH (Fig. 8 upper right panel), which is influenced by the competitive FRB and SRB reactions as explained below. With the increase in pH, the accumulated Br ions at the microporosity domain are kicked out of the ferrihydrite surface to be replaced by hydroxyl ions, whereas with the decrease in pH, higher concentration of Br are attracted to the surface, as expected (see Fig. 7 to compare with pH trends).

As discussed by Sengor et al. [11], pH values initially show an increasing trend with depth followed by a slowly decreasing trend in the anoxic zone (Fig. 7, upper left). The initial increase with depth is controlled by the multiple enzyme-mediated reductive dissolution of ferrihydrite, which drives the pH up, as shown by (Sengor et al. [44]):

$$8Fe(OH)_{3(s)} + CH_3COOH + 14H^+ \rightleftharpoons 8Fe^{2+} + 2HCO_3^- + 20H_2O \quad (11)$$

The decreasing trend at about 10 cm depth is due to the microbially mediated sulfate reduction by SRB, as shown in Table 2 by:

$$CH_3COO^- + SO_4^{2-} \rightleftharpoons 2CO_3^{2-} + HS^- + 2H^+ \quad (12)$$

Model results of this study show that when EDL effects are implemented in the code, pH shows a further decreasing trend with depth (dotted lines in Fig. 7), compared to the "no_EDL" case (solid lines in Fig. 7). This is due to the higher precipitation of $FeS_{(s)}$ in the presence of EDL implementation (Fig. 11, lower left), consistent with the lower concentration profile of Fe(II) observed in the presence of EDL (Fig. 7, lower right; Fig. 10). As the total Fe is mainly in the form of Fe(II) species, the positive surface of ferrihydrite (at the considered pH ranges) excludes the majority of Fe(II) from the EDL, leaving high concentration of Fe(II) in the macroporosity layer available to precipitate as $FeS_{(s)}$ with the available aqueous sulfide ions in this layer. On the other hand, the concentration profiles of Pb (Fig. 7, lower left panel) and Zn (Fig. 8, lower panels; Fig. 9) show higher computed concentrations with depth along with the implementation of EDL. This is partly due to the desorption of heavy metals from ferrihydrite surface due to the lower pH, and partly due to the formation of strong metal (bi)sulfide complexes after the production of biogenic sulfide by SRB in the anoxic zone. Again, as more strong aqueous metal (bi)sulfide complexes are retained within the microporosity domain (black lines in Fig. 8, lower panels), the availability of free metals to form metal sulfide precipitates decreases, which is again consistent with the corresponding delays in metal sulfide formation (compare dotted and solid black lines in Fig. 11). These results reveal the significance of EDL implementation, in addition to MCD effects, in simulating the heavy metal fate and transport problems using coupled complex reaction network environments to avoid any underestimation of the mobility of heavy metals in the system.

To illustrate the competitive effects of the strong metal (bi)sulfide complexes on pH and coupled biogeochemical reactions, model simulations are run considering "low" and "high" rates of sulfate and Fe(III) reduction, respectively, considering 5% EDL in all cases. The results show that when Fe(III) reduction rate is increased, the rise in pH (caused by the 1st reaction mentioned above) is more pronounced and the decrease in pH (caused by the second reaction mentioned above) is less pronounced (blue lines in Fig. 7, upper left). If the sulfate reduction rate is lowered, then pH increases due to the lower amount of sulfide production and hence lower amount of FeS precipitation (red lines in Fig. 7, upper left; Fig. 11, lower left). The rise in pH increases the net sorption of metals onto ferrihydrite surface. Aqueous metal (bi)sulfide complex formation as well as the metal sulfide precipitation formation potential decreases. As a result of the net effect of these reactions, the dissolved heavy metal concentrations decrease with time and depth. Although both the "low" and "high" rates of sulfate and Fe(III) reduction cases increase the pH of the medium, the system is more sensitive to the changes in Fe(III) reduction compared to sulfate reduction, which is in accordance of the stoichiometry of the reactions. As there is less production of sulfide with lower SRB activity, the impact of aqueous metal (bi)sulfide complexes gets minimal as the rate of SRB activity decreases. In the case of higher Fe(III) reduction, the increase in pH results in the negatively charged (bi)sulfide complexes to be excluded from the EDL layer (due to the abundance of hydroxyl ions at the positive ferrihydrite surface kicking off the negatively charged ions) and thus significantly enhancing their precipitation as metal sulfides at the macroporosity layer.

5 Summary and conclusions

The present study aims at the investigation of species-specific multicomponent diffusion (i.e., Nernst-Planck representation of diffusion compared, using Table 6, versus the uniform Fickian diffusion of species in the sediments) and the explicit treatment of electrostatic effects, on the overall dynamics of biogeochemical cycling of metals in example diffusive transport-dominated lake sediments of LCdA. The impact of MCD and EDL on reactive transport and sorption of heavy metals in a *natural environment*, integrating coupled biotic reaction network with multiple terminal electron acceptors is presented for the first time to the authors' knowledge. The solute benthic fluxes at the LCdA sediments are controlled by diffusion. In such purely diffusive transport-dominated systems, the electrochemical potential of species in the system can play an important role in determining the rates of diffusion of ions in pore water, in addition to pure Fickian processes, which would thus impact the overall biogeochemical dynamics. The results of the study reveal that the use of single uniform diffusion coefficient for all species in purely diffusion-dominated sediments may underestimate the mobility of heavy metals undergoing complex reaction network. This outcome is further signified when explicit treatment of EDL effects is considered in addition to MCD. The simulation results also illustrate the importance of aqueous metal (bi)sulfide complexes, especially when MCD and EDL effects are implemented in reactive transport simulations, impacting the solubility and dynamics of heavy metals in diffusion-dominated systems. The competitive effects of FRB and SRB activities on pH and overall biogeochemical processes showed that the system is more sensitive to the changes in Fe(III) reduction compared to sulfate reduction. The impact of EDL implementation (in addition to MCD) using a wide range of microporosity spectrum is also assessed on the overall ion transport dynamics in the system, demonstrating the significance of accurate determination of EDL layer, based on the ionic strength of the solution. Investigations are underway to increase the model complexity in a step-by-step fashion in later stages of the model to cover the dynamics of additional heavy metals of interest (e.g., As, Mn, Cu) and larger scale processes. Other future work also includes conducting numerical simulations for different sediments in natural environments, or different regions of LCdA environment, to seek representation of processes pertaining to different regions.

References

1. Gevao, B., Hamilton-Taylor, J., Murdoch, C., Jones, K.C., Kelly, M., Tabner, B.J.: Depositional time trends and remobilization of PCBs in lake sediments. Environ. Sci. Technol. **31**, 3274–3280 (1997)
2. Santschi, P.: Radionuclides as tracers for sedimentation and remobilization. In: Sly, P.G. (ed.) Sediments and water interactions, pp. 437–449. Springer-Verlag, New York (1986)
3. Gallon, C., Tessier, A., Gobeil, C., Alfaro-De La Torre, M.C.: Modeling diagenesis of lead in sediments of a Canadian Shield lake. Geochim. Cosmochim. Acta. **68**(17), 3531–3545 (2004)
4. Canavan, R.W., Van Cappellen, P., Zwolsman, J.J.G., Van den Berg, G.A., Slomp, C.P.: Geochemistry of trace metals in a freshwater sediment: field results and diagenetic modeling. Sci. Total Environ. **381**(1), 263–279 (2007)
5. Wu, G., Li, L.Y.: Modeling of heavy metal migration in sand/bentonite and the leachate pH effect. J. Contam. Hydrol. **33**(3), 313–336 (1998)
6. Boyle, J.: Redox remobilization and the heavy metal record in lake sediments: a modeling approach. J. Paleolimnol. **26**(4), 423–431 (2001)
7. Couture, R.M., Shafei, B., Van Cappellen, P., Tessier, A., Gobeil, C.: Non-steady state modeling of arsenic diagenesis in lake sediments. Environ. Sci. Technol. **44**(1), 197–203 (2009)
8. Torres, E., Ayora, C., Jiménez-Arias, J.L., García-Robledo, E., Papaspyrou, S., Corzo, A.: Benthic metal fluxes and sediment diagenesis in a water reservoir affected by acid mine drainage: a laboratory experiment and reactive transport modeling. Geochim. Cosmochim. Acta. **139**, 344–361 (2014)
9. Torres, E., Couture, R.M., Shafei, B., Nardi, A., Ayora, C., Van Cappellen, P.: Reactive transport modeling of early diagenesis in a reservoir lake affected by acid mine drainage: trace metals, lake overturn, benthic fluxes and remediation. Chem. Geol. **419**, 75–91 (2015)
10. Torres, E., Galván, L., Cánovas, C.R., Soria-Píriz, S., Arbat-Bofill, M., Nardi, A., Papaspyrou, S., Ayora, C.: Oxycline formation induced by Fe (II) oxidation in a water reservoir affected by acid mine drainage modeled using a 2D hydrodynamic and water quality model—CE-QUAL-W2. Sci. Total Environ. **562**, 1–12 (2016)
11. Şengör, S.S., Spycher, N.F., Ginn, T.R., Sani, R.K., Peyton, B.: Biogeochemical reactive–diffusive transport of heavy metals in Lake Coeur d'Alene sediments. Appl. Geochem. **22**(12), 2569–2594 (2007)
12. Van Cappellen, P., Gaillard, J.-F.: Biogeochemical dynamics in aquatic sediments. In: Lichtner, P.C., Steefel, C.I., Oelkers, E.H. (eds.) Reactive transport in porous media, pp. 335–376. Mineralogical Society of America, Washington, D.C. (1996)
13. Boudreau, B.P.: Diagenetic models and their implementation. Modeling transport and reactions in aquatic sediments. Springer-Verlag, Heidelberg (1997)
14. Appelo, C.A.J., Wersin, P.: Multicomponent diffusion modeling in clay systems with application to the diffusion of tritium, iodide, and sodium in Opalinus clay. Environ. Sci. Technol. **41**(14), 5002–5007 (2007)
15. Appelo, C.A.J., Van Loon, L.R., Wersin, P.: Multicomponent diffusion of a suite of tracers (HTO, Cl, Br, I, Na, Sr, Cs) in a single sample of Opalinus clay. Geochim. Cosmochim. Acta. **74**(4), 1201–1219 (2010)
16. Ghorayeb, K., Firoozabadi, A.: Modeling multicomponent diffusion and convection in porous media. SPE J. **5**(02), 158–171 (2000)
17. Furrer, G., Wehrli, B.: Microbial reactions, chemical speciation, and multicomponent diffusion in porewaters of a eutrophic lake. Geochim. Cosmochim. Acta. **60**(13), 2333–2346 (1996)
18. Liang, Y., Richter, F.M., Chamberlin, L.: Diffusion in silicate melts: III. Empirical models for multicomponent diffusion. Geochim. Cosmochim. Acta. **61**(24), 5295–5312 (1997)
19. Fornasiero, F., Prausnitz, J.M., Radke, C.J.: Multicomponent diffusion in highly asymmetric systems. An extended Maxwell-Stefan

model for starkly different-sized, segment-accessible chain molecules. Macromolecules. **38**(4), 1364–1370 (2005)
20. Désilets, M., Proulx, P., Soucy, G.: Modeling of multicomponent diffusion in high temperature flows. Int. J. Heat Mass Transf. **40**(18), 4273–4278 (1997)
21. Giovangigli, V.: Multicomponent flow modeling. Sci. China Math. **55**(2), 285–308 (2012)
22. Wang, Y., Van Cappellen, P.: A multicomponent reactive transport model of early diagenesis: application to redox cycling in coastal marine sediments. Geochim. Cosmochim. Acta. **60**(16), 2993–3014 (1996)
23. Zorrilla, S.E., Rubiolo, A.C.: A model for using the diffusion cell in the determination of multicomponent diffusion coefficients in gels or foods. Chem. Eng. Sci. **49**(13), 2123–2128 (1994)
24. Cussler, E.L.: Multicomponent diffusion. Elsevier (2013)
25. Turner, J.S.: Double-diffusive phenomena. Annu. Rev. Fluid Mech. **6**(1), 37–54 (1974)
26. Parkhurst, D.L., Appelo, C.A.J.: Description of input and examples for PHREEQC version 3: a computer program for speciation, batch-reaction, one-dimensional transport, and inverse geochemical calculations (No. 6-A43). US Geological Survey (2013)
27. Appelo, C.A.J., Vinsot, A., Mettler, S., Wechner, S.: Obtaining the porewater composition of a clay rock by modeling the in-and out-diffusion of anions and cations from an in-situ experiment. J. Contam. Hydrol. **101**(1), 67–76 (2008)
28. Muniruzzaman, M., Rolle, M.: Impact of multicomponent ionic transport on pH fronts propagation in saturated porous media. Water Resour. Res. **51**(8), 6739–6755 (2015)
29. Bear, J.: Dynamics of fluids in porous materials. Society of Petroleum Engineers (1972)
30. Bard, A.J., Faulkner, L.R.: Fundamentals and applications. Electrochem. Methods. **2**, (2001)
31. Steefel, C.I., Maher, K.: Fluid-rock interaction: a reactive transport approach. Rev. Mineral. Geochem. **70**, 485–532 (2009). https://doi.org/10.2138/rmg.2009.70.11
32. Steefel, C.I., Mayer, K.U., Arora, B., Appelo, C.A.J., Hammond, G., Jacques, D., Kolditz, O., Lagneau, V., Lichtner, P.C., Meussen, H., Molins, S., Parkhurst, D.L., Shao, H., Simůnek, J., Van der Lee, J., Yabusaki, S.B., Yeh, G.T.: Reactive transport codes for subsurface environmental simulation. Comput. Geosci. (2014) submitted
33. Alt-Epping, P., Tournassat, C., Rasouli, P., Steefel, C.I., Mayer, K.U., Jenni, A., Mäder, U., Sengor, S.S., Fernández, R.: Benchmark reactive transport simulations of a column experiment in compacted bentonite with multispecies diffusion and explicit treatment of electrostatic effects. Comput. Geosci. **19**(3), 535–550 (2015)
34. Steefel, C.I., Yabusaki, S.B., Mayer, K.U.: Reactive transport benchmarks for subsurface environmental simulation. Comput. Geosci. **19**(3), 439 (2015)
35. Ullman, W.J., Aller, R.C.: Diffusion coefficients in nearshore marine sediments. Limnol. Oceanogr. **27**(3), 552–556 (1982)
36. Balistrieri, L.S.: Preliminary estimates of benthic fluxes of dissolved metals in Coeur d'Alene Lake, Idaho. US Department of the Interior, US Geological Survey (1998)
37. Winowiecki, L.: Geochemical cycling of heavy metals in the sediment of Lake Coeur d'Alene, Idaho. Masters Thesis, University of Idaho, Moscow, Idaho (2002)
38. Russell, E.W.: Soil conditions and plant growth, 473p. Longmans Publishing, London (1973)
39. Parkhurst, D.L., Appelo, C.A.J.: User's guide to PHREEQC (version 2)—a computer program for speciation, batchreaction, one-dimensional transport, and inverse geochemical calculations. US Geol. Surv. Water-Resour. Investig. Rep. 99-4259, Denver, CO (1999)
40. Doussan, C., Poitevin, G., Ledoux, E., Detay, M.: River bank filtration: modelling of the changes in water chemistry with emphasis on nitrogen species. J. Contam. Hydrol. **25**, 129–156 (1997)
41. Brugato, C., 1999. Mathematical modeling of an anaerobic syntrophic butyrate-degrading coculture. Masters Thesis, University California, Davis
42. Arora, B., Şengör, S.S., Spycher, N.F., Steefel, C.I.: A reactive transport benchmark on heavy metal cycling in lake sediments. Comput. Geosci. **19**(3), 613–633 (2015)
43. Buffle, J., Zhang, Z., Startchev, K.: Metal flux and dynamic speciation at (bio) interfaces. Part I: critical evaluation and compilation of physicochemical parameters for complexes with simple ligands and fulvic/humic substances. Environ. Sci. Technol. **41**(22), 7609–7620 (2007)
44. Şengör S.S., Spycher N., Ginn T.R., Moberly J.G., Peyton B., Sani R.K., 2007. Reductive dissolution and metal transport in Lake Coeur d'Alene sediments. In Water-rock interaction, WRI-12 (Bullen T. and Wang Y., eds.), vol. 2. Taylor & Francis Group, London, pp. 895–899